Hindawi
Journal of Nanomaterials
Volume 2023, Article ID 8564161, 11 pages
https://doi.org/10.1155/2023/8564161

Research Article

Fractal Dimension Image Processing for Feature Extraction and Morphological Analysis: Gd^{3+}/13X/DOX/FA MRI Nanocomposite

Sadegh Ghaderi

Department of Neuroscience and Addiction Studies, School of Advanced Technologies in Medicine, Tehran University of Medical Sciences, Tehran, Iran

Correspondence should be addressed to Sadegh Ghaderi; s_ghaderi@razi.tums.ac.ir

Received 13 February 2023; Revised 10 March 2023; Accepted 16 March 2023; Published 21 April 2023

Academic Editor: Mazeyar Parvinzadeh Gashti

One of the most fundamental subjects in nanoscience and nanotechnology is structural analysis. We employed a scanning electron microscope (SEM) image of the manufactured Gd^{3+}/13X/DOX/FA nanocomposite in this study. The size, dimensions, and morphology of nanocomposite materials were studied to ensure the uniformity and homogeneity of SEM images. This is the first study to look at segmented SEM images for fractal dimension (FD) and other statistical criteria, including average, maximum, minimum, skewness, and range for magnetic resonance imaging (MRI) nanocomposite. The average of FD (FD_{avg}), the standard deviation of FD (FD_{sd}), and the lacunarity of FD (FD_{lac}) fractal data analysis criteria were also employed. The findings show that particle sizes and shapes vary because the minimum-to-maximum range is not zero, and our data provide a reasonable range. This interpretation is further supported by an analysis of the nanocomposite's SEM image. At first glance, the image seemed to be uniform. However, when the calculations were performed, it was discovered that the generated particles were not particularly uniform. The particles were uniformly dispersed throughout all surfaces, although their sizes, dimensions, and morphologies varied. In conclusion, the study was supported by fractal data analysis, emphasizing the importance of structural analysis for future research, particularly for medical applications like MRI.

1. Introduction

The powers of structural, directional, and functional control are the most essential issues in nanoscience and emerging nanotechnology. Many attempts have been made to regulate the spatial distribution of nanoparticles (NPs) as well as their physical and functional features [1–3].

Magnetic resonance imaging (MRI) is a noninvasive and novel imaging modality [4–6]. The use of contrast agents (CAs) in MRI is offered to enhance image contrast as well as the identification of diseased cells [7]. Magnetic NPs are one of the primary types of nanoscale materials that have the potential to fundamentally alter current diagnostic and treatment approaches [8, 9].

The scanning electron microscope (SEM) is a technique that is used to scan and analyze microscopic characteristics on solid surfaces, as in MRI CAs. SEM images are often used to qualitatively analyze the surface features of morphological variables like size, surface composition, and shape of samples. They are also used to find sample characteristics like compositional changes, topography (shape, inclination, edges, etc.), and physical differences (crystalline structure, magnetic fields, electrical fields, etc.) [1, 6, 10].

Image processing of nanostructures involves a variety of preparations, subdivisions, and data preprocessing processes that end in quantitative data extraction. Recently, computer-based image-processing techniques have advanced significantly, allowing for the quantitative representation of complex hues, patterns, texture properties, and sizes. According to research done in the past, computer-aided diagnostics and image analysis may be some of the best screening methods because they make it easier to process large amounts of information [10–13].

Fractal geometry is a mathematical method that is used to analyze irregular geometric shapes. The fractal dimension (FD) may show some of the properties of natural imagery [11–14].

Calculating the predictable edge of the length acquired along the border and the number of ladders characterizes the FD parameter [14–21]. Because lower step sizes represent the existence of more features on the particle output, the boundary length rises as the step size is reduced [11, 22–24]. Furthermore, incorporating other metal cations (such as gadolinium (Gd^{3+})) into the nanosized zeolites may alter their behavior, raising interest in zeolite NP as an imaging tool [26]. It is possible that this is a strong argument for the fractal analysis of images [25].

Gd^{3+}-based MRI CAs have the best structure for producing a positive signal, or T1 CA. Because of its low toxicity, good solubility, great physicochemical qualities, and high relaxation, it is also commonly employed in clinical diagnostics to promote the relaxation of water protons. Also, using Gd^{3+} nanocomposite, which is paramagnetic, may slow down the rate of relaxation and improve contrast [26–28].

Doxorubicin (DOX) is an anticancer medication that has the potential to be used against a variety of cancers. The folic acid receptor is utilized to target materials in MRI CAs because of folic acid's high absorption and toxicity promote binding to its receptor on the surface of cancer cells. The CA structure, which we presented in the prior work, was targeted with doxorubicin and folic acid [29–31].

Zeolite has a microporous structure made up of crystalline aluminosilicate and specific chemical forms and is widely employed for three major properties: adsorption, ion exchange, and catalytic properties. Zeolite, particularly zeolite 13X, has a crystalline structure and a hydrated aluminum main framework with a hole filled with water particles and ions. Previous research has focused on two forms of zeolites, X and A [32–35]. Tatlier and Erdem-Çenatalar [33] estimated the value of the FD of the 13X zeolite in the following earlier reports: 2.08. Finally, in this study, we will use the SEM image of the Gd^{3+}/13X/DOX/FA nanocomposite [6].

According to our findings, no FD research has been conducted on MRI-Gd-based CAs. Furthermore, there are substantial differences across related research regarding the type and structure of the contrast material used and the SEM image processing technique employed. Also, the FD method on a manufactured MRI nanocomposite with anticancer and targeting properties, Gd^{3+}/13X/DOX/FA nanocomposite, will be performed for the first time [6].

Our work is valuable because we perform preprocessing operations to improve image quality, automatic image segmentation to remove human error interference, and statistical data calculations using a more user-friendly application. The purpose of this work is to investigate the size, dimensions, and morphology of synthesized Gd^{3+}/13X/DOX/FA nanocomposite at the molecular level to confirm or reject the uniformity and homogeneity of SEM images of nanocomposites based on the range of particles. Consequently, it is important to examine the support for FD analysis, underlining the significance of structural analysis on nanocomposites for future study, especially for medical applications.

2. Methods

2.1. Nanocomposite and Summary of Methods. Ghaderi et al. [6] developed the Gd^{3+}/13X/DOX/FA. X-ray diffraction (XRD) patterns and SEM images were applied to determine the physicochemical parameters of the Gd^{3+}/13X/DOX/FA nanocomposite. Lashgari et al. [14] assessed the FDs of 30 randomly selected SEM images (manganese–chromium bimetallic nanocomposite) using MATLAB software. Lastly, the SPSS software was used to acquire the image's histogram and normalize the image's histogram, mean, median, maximum and minimum values, range, skewness, and harmonic mean. In this study, however, based on prior research, 30 random images are needed after applying the pre-processing SEM image in Gd^{3+}/13X/DOX/FA nanocomposite using the automated segmentation approach through the toolbox and MATLAB program. Then, using Excel, we will determine the average of FD (FD_{avg}), standard deviation of FD (FD_{sd}), and lacunarity of FD (FD_{lac}) for all images, as well as the average, maximum, minimum, skewness, and range of the chosen images. Lacunarity has been developed to distinguish between distinct texture appearances that may have the same FD value. Lacunarity quantifies the distribution of gap sizes: geometric objects with low lacunarity are homogenous since all gap sizes are the same, while objects with high lacunarity are heterogeneous [36, 37]. For the first time, our image processing research relies on a synthetic MRI nanocomposite with anticancer and targeting characteristics.

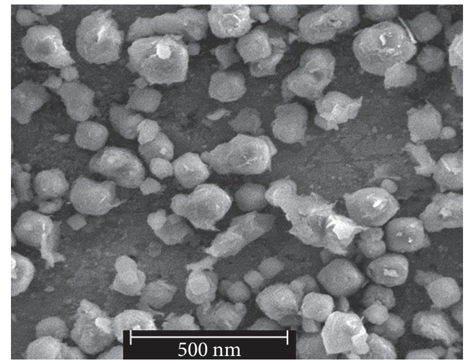

FIGURE 1: SEM image of (Gd^{3+}/13X/DOX/FA) nanocomposite.

2.2. Calculation of FD and Image Analysis. Dimension is one of the most important concepts in fractal geometry [38]. Currently, numerous FD analysis and computation methods have been followed by comparable bases, which are briefly summarized in three steps:

(i) Object quantification using various step sizes and stages.
(ii) Values were measured against the size of the steps, and the minimum squares of the regression line across data points were determined.
(iii) Estimating FDs as a regression line slope.

We will employ the box-counting approach in our research since the box-counting dimension [14] is a mathematical design, and an estimate of the box-counting dimension is simple. This value has become one of the most commonly used generic dimensions [39, 40]. We used MATLAB version r2022b to do the FD assessments and analyses. The SEM image of the

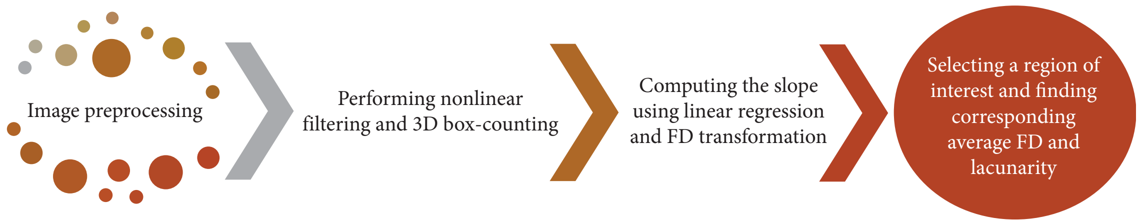

Figure 2: The flow diagram of the proposed algorithm.

Gd^{3+}/13X/DOX/FA nanocomposite is shown in Figure 1. This image will be used in the image processing section [6].

2.3. FD Methodical Concepts. Fractals may be defined numerically as a geometrical set with a Hausdorff–Besicovitch measurement that carefully exceeds the topological measurement. Mandelbrot [41] used the word "fractal" to describe non-Euclidean structures that exhibit self-similarity at different sizes. Because most organic and common highlights include discontinuities and fractures, they will have an FD. In the same way, most of these regular structures are complicated and sometimes have a precise Euclidean (smooth) form so that they can be approximated accurately.

In Euclidean n-space, a restricted set S is manifestly self-comparable if it is the union of Nr no overlapping subsets as for a scaling factor r, each of which has the structure $r(Sn)$, where the Nr and Sn sets are consistent in circulation to S. As a result, the Hausdorff–Besicovitch—the fractal measurement—of a finite set S in Rn is a legitimate number used to depict the geometric multidimensional character of S in the same way that length is employed as an estimating tool in Euclidean (discrete) space. Nr is simply the number of comparable (invariant) shapes, and r is the scaling factor for comparison [42, 43]. The FD may now be calculated in Equation (1) as follows:

$$\mathrm{FD} = \frac{\log(Nr)}{\log\left(\dfrac{1}{r}\right)}. \tag{1}$$

In reality, most regular and some numerical self-comparable fractals are arbitrary, meaning that they scale accurately. The similarity between shapes seen at different scales in conventional fractals is often inexact and seen as irregular rather than self-comparable. In general, the FD of an investigated structure should have self-comparable split and sporadic forms that do not change as the size of the estimate goes up or down, all the way up to infinity.

Depending on the goals and profundity of the acquired image, this must be true for a limited number of scales. So, for each studied typical fractal, there is a small scaling range below or above which the structure is either smooth (i.e., Euclidean) or completely rough and not self-comparable (i.e., arbitrary) [44].

To differentiate between two surfaces if their FD worth is indistinguishable despite the fact that the two surfaces are unlikely to be comparable, we must calculate the lacunarity of the FD surface. Lacunarity quantifies the "knottiness" of fractal information, providing meta-data on the figured FD values in the image. The greater the lacunarity, the more inhomogeneous the investigated fractal region, and vice versa [45].

It is defined in terms of the fraction of the difference over the mean capacity estimate, as in, where M and N are the sizes of the FD-produced images [46–48] (Equation (2)):

$$\text{Lacunarity} = \frac{\frac{1}{MN}\sum_{m=0}^{M-1}\sum_{n=0}^{N-1} I(m,n)^2}{\left(\frac{1}{MN}\sum_{k=0}^{M-1}\sum_{l=0}^{N-1} I(k,l)\right)^2} - 1. \tag{2}$$

2.4. General Schema of the Proposed Algorithm. As can be seen from Figure 2, the algorithm consists of four general stages. The first step is to read and preprocess the SEM image. The second step is to perform nonlinear filtering on a pixel block of varying sizes (box counting). The third step is to compute the slope using linear regression, and finally, in the last step, selecting a ROI and finding the corresponding average FD and lacunarity are applied.

2.5. Image Preparation. The image evaluation process is separated into many parts. The first stage is the handling step, in which all arrangements of SEM image groups are generated for each instance in computerized imaging and correspondence in version design (DICOM image) and then translated to FD values for each pixel. The FD shift produced images with much higher contrast than the originals, as well as easier SEM image segmentation.

At this point, the fractal analysis is performed to find the most severe normalized FD (FD_{avg})—a normalized FD value is obtained for each image in time sequence, and the biggest is chosen—along with its comparative lacunarity (i.e., level of inhomogeneity). Finally, an apparent structure is used to study the influence of SEM logistical factors on FD_{avg} and lacunarity. All of the steps are generally divided into four categories:

(1) Image preprocessing.
(2) FD transformation.
(3) Region of interest (ROI) and feature extraction.
(4) FD_{avg} and lacunarity calculations.

2.6. Image Preprocessing. The proposed design was performed through image reading. The process of preprocessing is described below.

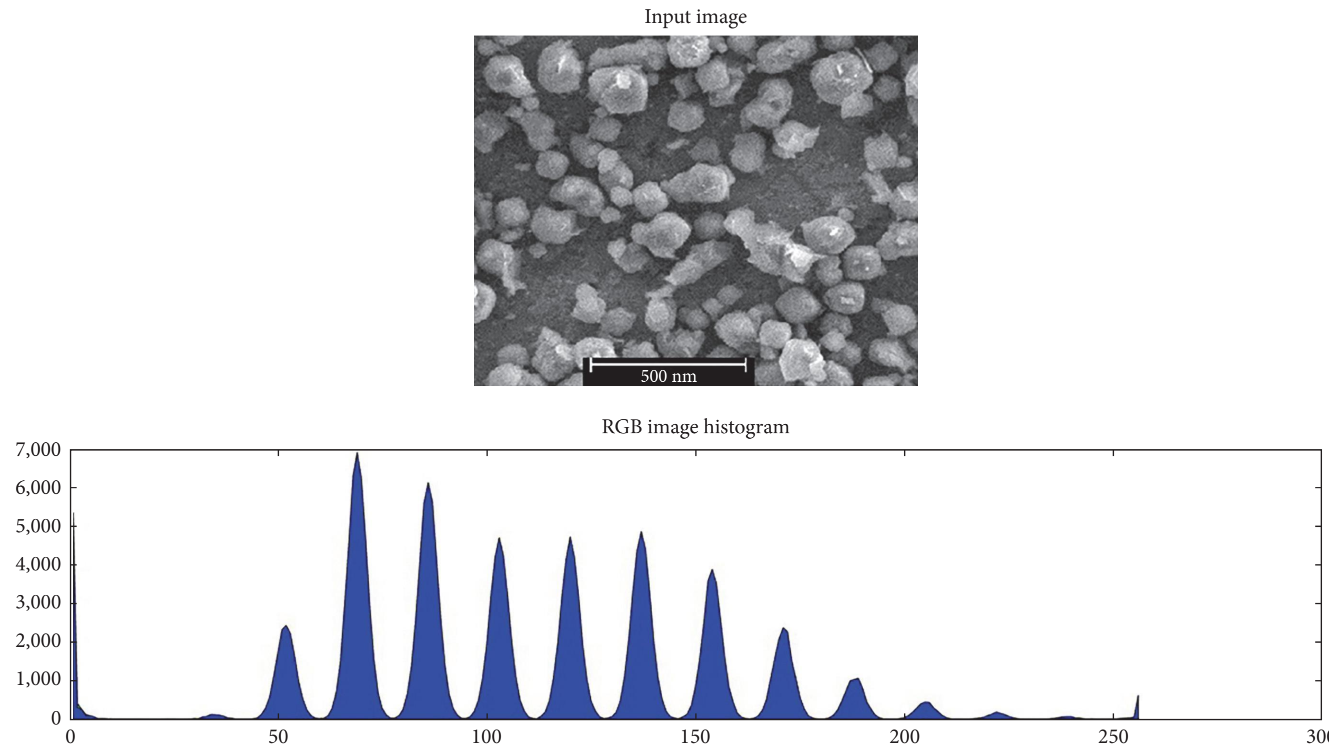

FIGURE 3: Input SEM images with their histogram.

2.6.1. Grayscale Conversion. After interpreting the SEM image, the image is grayed out in this stage.

2.6.2. Histogram Equalization. The histogram equalization function improves image quality. Histogram equalization is a method for enhancing contrast by altering image intensities. Figures 3 and 4 show the histograms of the original and enhanced images, respectively.

2.6.3. Segmentation. Segmentation is the process of labeling each pixel. In other terms, segmentation divides a digital image into several segments called "pixels." The purpose of segmentation is to reduce an image's representation into something more relevant and simpler to examine. Image segmentation produces a collection of segments that encompass the full image or a set of contours taken from the image. The threshold approach is the most basic method of image segmentation. The choice of a thresholding method depends on the specific characteristics of the image being analyzed, such as the type of image, the distribution of pixel intensities, and the presence of noise or artifacts. There are many thresholding methods available, including global thresholding, adaptive thresholding, and Otsu's thresholding, among others. Global thresholding is the most basic method and involves selecting a fixed threshold value that separates the foreground and background pixels based on the pixel intensity values. To calculate the FD of an image using the box-counting method, first convert a grayscale image to a binary image. This approach uses a threshold value [49–51].

Otsu's thresholding method is a popular choice for this step, as it can automatically determine an optimal threshold value based on the pixel intensity distribution of the image. Once the image is binarized, it is divided into a grid of equal-sized boxes. The size of the boxes is varied over a range of scales, and for each scale, the number of boxes that contain at least one foreground (i.e., object) pixel is counted. The box counts are then plotted against the box size on a log–log scale. The slope of the resulting plot represents the FD of the image. To obtain a more accurate estimate of the FD, the box-counting procedure is typically repeated with multiple grid sizes, and the slope is calculated for each size range. The average of these slopes is then used as the final estimate of the FD. Finally, every pixel in an image is designated an object pixel if its value is more than the threshold value and a background pixel if its value is less than the threshold value. A "1" value is assigned to an object pixel, whereas a "0" value is assigned to a background pixel. Following that, a binary image containing all of the object and background pixels is produced (see Table 1) [49–53].

2.7. Performing Nonlinear Filtering on a Varying Size Pixel Block. Nonlinear image filtering is based on the idea that instead of utilizing the spatial mask in a convolution process, the mask is used to acquire nearby pixel values, and then ordering processes generate the output pixel. In other words, when the mask is moved around the image, the order of the pixels in the windowed area of the image is rearranged, and the output pixel is formed from the rearranged input pixels [54].

2.8. FD Transformation. The resulting SEM images are converted to FD images using the differential box-counting (DBC) technique at various scales, after which they are shown for ROI proof, followed by surface analysis. The DBC technique is often used when dealing with a large

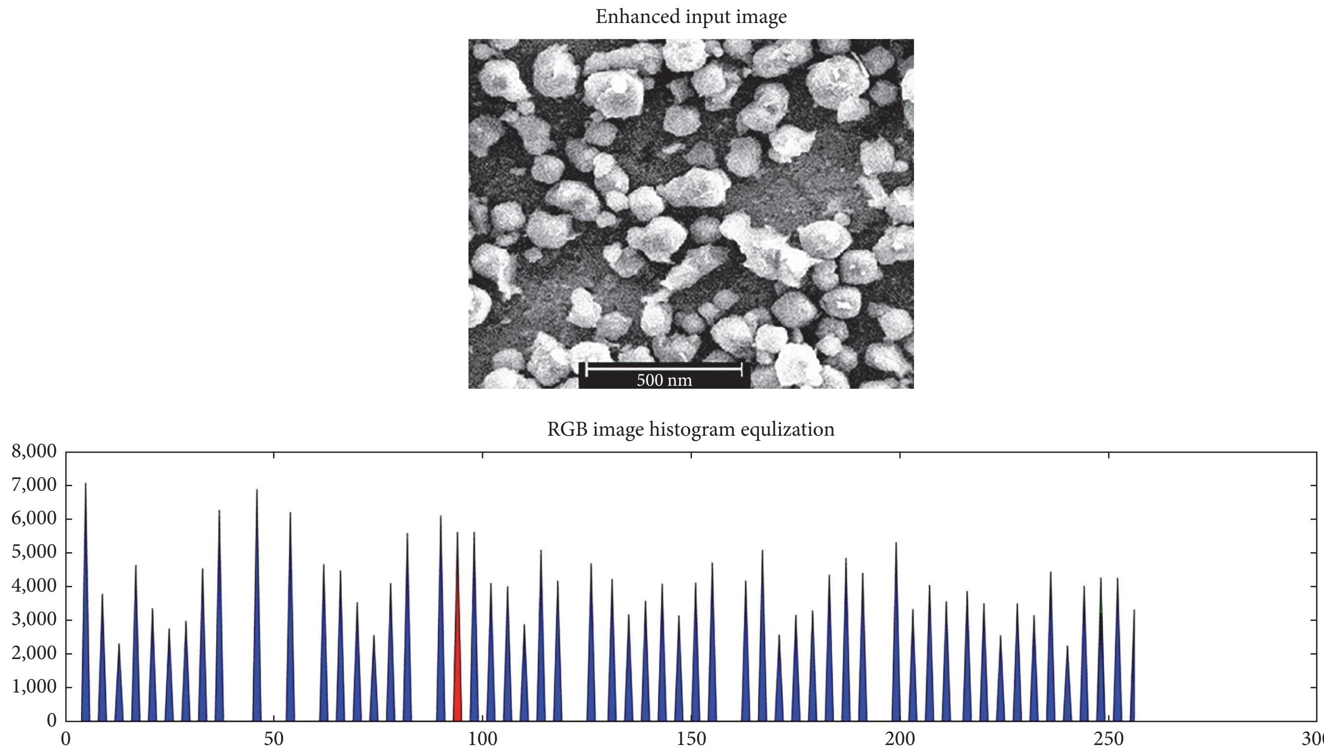

FIGURE 4: Enhanced SEM images with their histogram.

number of information values per test (the images below are all 512×512 pixels in size). In this study, both the DBC and fragmented Brownian movement computations were first attached to the images; nevertheless, the DBC method was chosen for the subsequent analysis since it performed faster on the FD counts of the 512×512 SEM images. The initial DICOM image $I(x, y)$ of size $M \times N$ is converted to an FD image by applying a varying-size nonlinear bit $w(s, t)$ of size $m \times n$ in Equation (3), which works by square preparation on the nearby pixels and determines the distinction between the most substantial ($p_{\max}$) and least significant ($p_{\min}$) force pixels. The two components and b are nonnegative whole values that are used to concentrate the bit $w(s, t)$ on the first picture's pixel p_{xy}. The component is determined in Equation (3) and connected in Equation (4) as follows:

$$w(s,t) = \sum_{s=-a}^{a} \sum_{t=-b}^{b} \text{floor}\left[\frac{p_{\max} - p_{\min}}{r}\right] + 1 \quad \text{where } r = 2, 3, 4, \ldots, j \qquad a = \text{ceil}\left(\frac{m-1}{2}\right), \qquad b = \text{ceil}\left(\frac{n-1}{2}\right), \tag{3}$$

where $d = 1, 2, 3, \ldots, j-1$ represents the number of boxes required to overlay the image on the grid $N_{d(x,\ y,\ d)}$. The scaling factor r was chosen experimentally to be between 2 and 9. In theory, r should indicate how much a certain pixel structure is self-like in its entirety.

$$N_{d(x,y,d)} = \sum_{s=-a}^{a} \sum_{t=-b}^{b} w(s,t) I(x+s, y+t) \left(\frac{j}{r}\right)^2. \tag{4}$$

2.9. Selecting a ROI and the Finding Corresponding Average FD and Lacunarity. After applying the previous steps and also using the output of the image segmentation stage (obtaining 30 sample images), each of the FD-average and lacunarity were calculated (Table 1).

3. Results and Discussions

Following the preprocessing and segmentation, 30 images from the SEM image were extracted (as described in the Methods section) to execute the fractal calculation procedure using MATLAB and Excel software. Table 1 shows the FD calculation (FD_{avg}, FD_{sd}, and FD_{lac}) results for 30 chosen SEM images. Table 2 shows the results of calculating the average, maximum, minimum, skewness, and range from the data in Table 1.

The variations within the pattern dimensions of the particles may be clearly seen, which reveals the nonhomogeneity of the created particles. Based on the obtained SEM image

Table 1: FD calculation for 30 images from the SEM image.

	1	2	3	4	5
		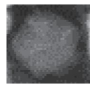		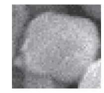	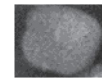
FD_{avg}	1.8309	1.8228	1.8291	1.9209	1.8538
FD_{sd}	0.5806	0.6359	0.5917	0.5238	0.6064
FD_{lac}	0.1003	0.1215	0.1045	0.0743	0.1069
	6	7	8	9	10
			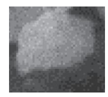	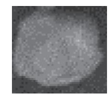	
FD_{avg}	1.8973	1.8393	1.8963	1.8593	1.9199
FD_{sd}	0.5719	0.5673	0.5451	0.5901	0.5679
FD_{lac}	0.0908	0.0950	0.0825	0.1006	0.0874
	11	12	13	14	15
			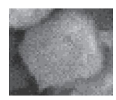	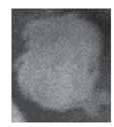	
FD_{avg}	1.8257	1.8681	1.8995	1.9163	1.8777
FD_{sd}	0.5267	0.6343	0.5100	0.6044	0.6855
FD_{lac}	0.0835	0.1151	0.0720	0.0994	0.1331
	16	17	18	19	20
			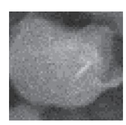		
FD_{avg}	1.9044	1.7623	1.8584	1.8564	1.8299
FD_{sd}	0.6244	0.5795	0.5961	0.5457	0.5301
FD_{lac}	0.1074	0.1081	0.1028	0.0864	0.0839
	21	22	23	24	25
		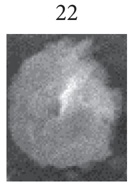		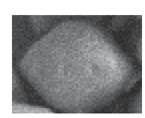	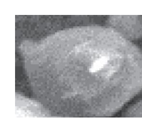
FD_{avg}	1.8042	1.8608	1.8043	1.8968	1.8250
FD_{sd}	0.5639	0.5548	0.5630	0.5805	0.5936
FD_{lac}	0.0976	0.0889	0.0973	0.0936	0.1058
	26	27	28	29	30
	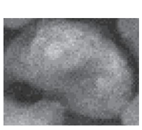		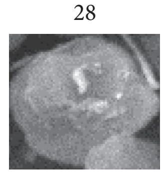	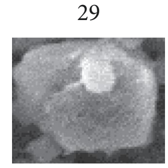	
FD_{avg}	1.8172	1.8713	1.8401	1.8453	1.8632
FD_{sd}	0.5422	0.5493	0.5333	0.5369	0.5436
FD_{lac}	0.0890	0.0861	0.0840	0.0846	0.0851

Table 2: Fractal data analysis of FD_{avg}, FD_{sd}, and FD_{lac} for SEM image.

Type	Average	Min	Max	Skewness	Range
FD_{avg}	1.85655	1.7623	1.9209	−0.13904	0.1586
FD_{sd}	0.572647	0.510	0.6855	0.871649	0.1755
FD_{lac}	0.095583	0.0720	0.1331	0.730874	0.0611

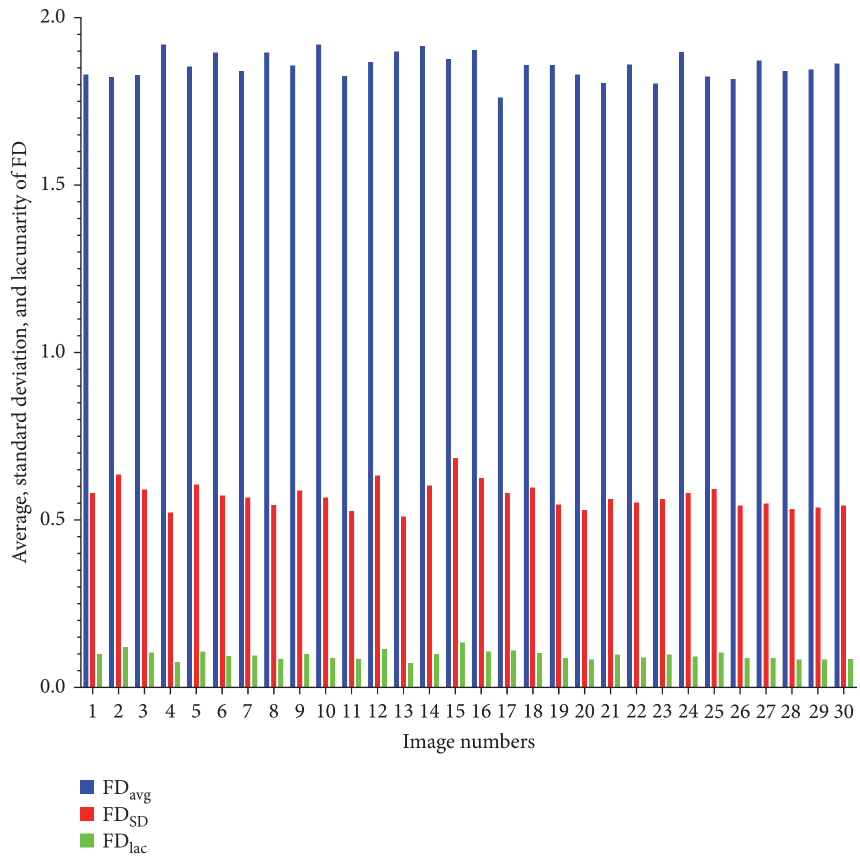

Figure 5: The chart shows that the FD calculation of 30 images.

information in Tables 1 and 2, Figure 5 shows a chart in which there are 30 particles, which range from 1.7623 to 1.9209, 0.510 to 0.6855, and 0.0720 to 0.1331 for FD_{avg}, FD_{sd}, and FD_{lac}, respectively.

The SD is a term that describes the scattering of data in a collection, and it is, therefore, one of the most significant statistical scales in the area of descriptive statistics. We can say that the SD represents the amount of data dispersion from the average point if the average estimations of the data distribution's center point are a set. Figures 6–8 show the FD_{avg}, FD_{sd}, and FD_{lac} for each of the 30 images.

Skewness is another statistical criterion for symmetry distribution probability. Skewness is the degree of distortion in the probability distribution's symmetric bell curve. To varying degrees, the distributions may be found on the right (positive) or left (negative). The derived statistical FD_{avg}, skewness = –0.13904, is therefore based on the selection criteria in Table 2. Distributions may also be skewed to the left (negatively) or pulled to lower values.

To evaluate for errors in the normal distribution, normal probability plots were created. If the plot points were in a straight line, normally distributed errors are assumed. In Figure 9, a typical quantile–quantile (Q–Q) plot is used to compare the forms of distributions, where the vertical axis quantiles the deviation from normal and the horizontal axis quantiles the observed values. Linearly linked points in the normal distribution mode suggest that the data are normally distributed.

As shown in Figure 9, the FD distribution of the nanocomposite particles is a regularly distributed error. Further, a residuals curve is a helpful tool for illuminating the data's fit to the model. To visualize the most prevalent forms of imbalance, a scatter plot of residuals vs. their matching fitted values may be constructed. The points and curve should be

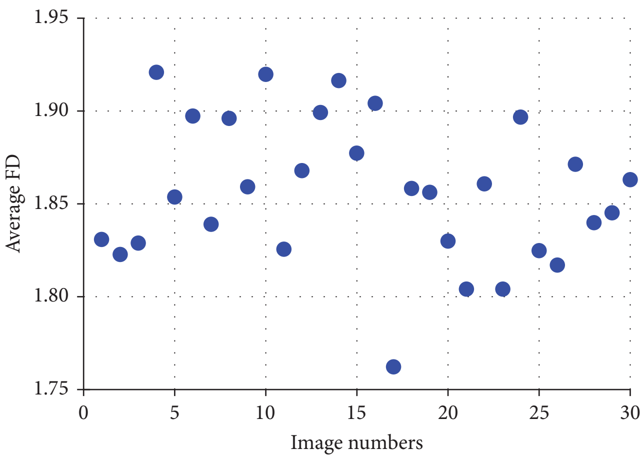

Figure 6: FD_{avg} for each image.

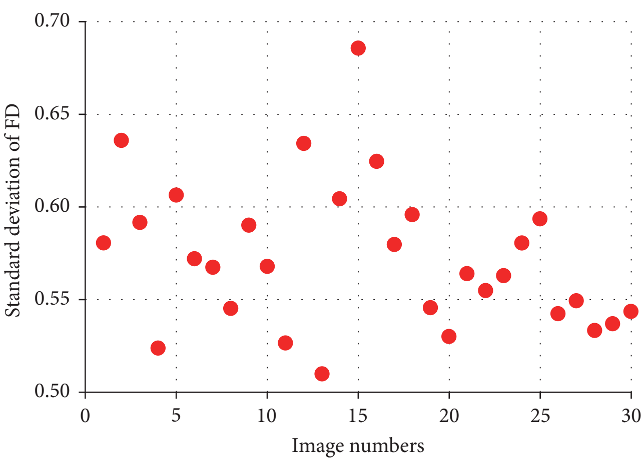

Figure 7: FD_{sd} for each image.

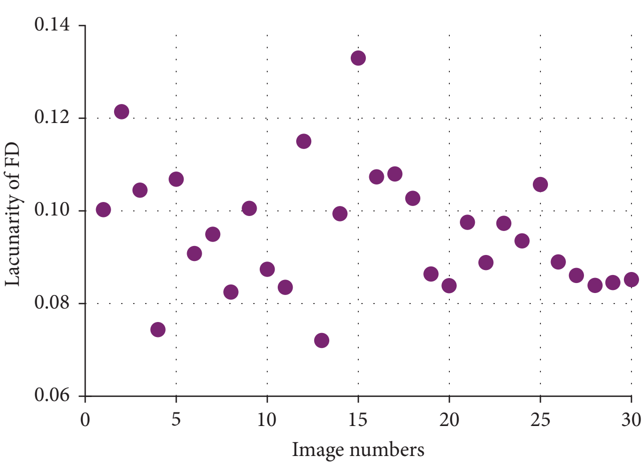

Figure 8: FD_{lac} for each image.

evenly spaced and symmetrical if the fitted model is correct. If the fitted model is acceptable, the curve in a detrended normal *Q*–*Q* plot of average should be symmetrical, and the points should be equally distributed. Figure 10 shows that

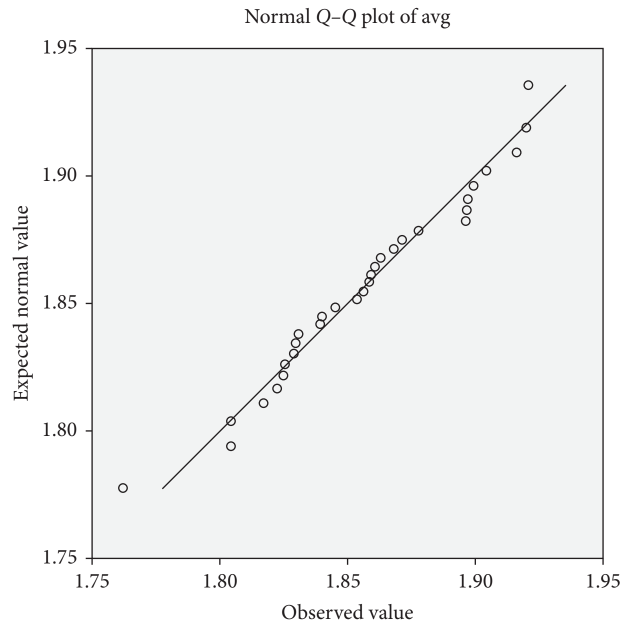

Figure 9: Normal probability curve of the FD_{avg} data SEM image.

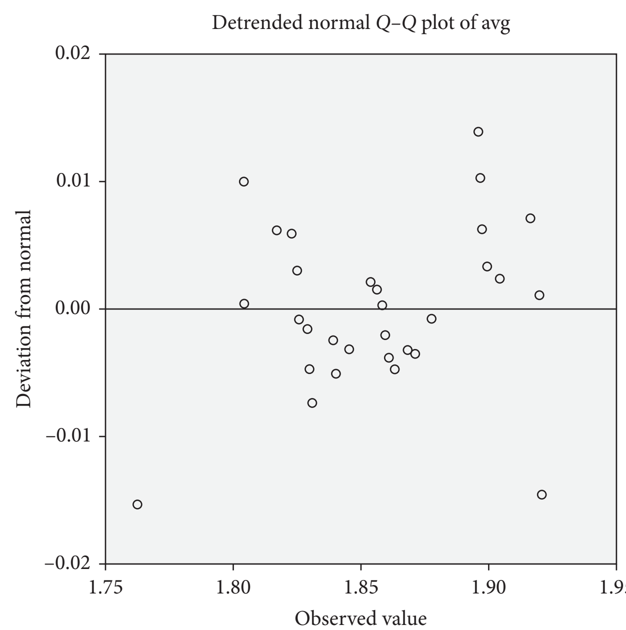

Figure 10: Detrended normal *Q*–*Q* plot of nanocomposite SEM image.

the points are not evenly distributed, accepting and revealing an asymmetric curve with a skewness of −0.13904.

Therefore, the comparison of results based on FD_{avg} shows that the mean and median of our synthesized NPs were larger. The range of synthesized NPs is closer to zero, indicating that the morphology and fabrication of NPs were more homogenized. The particle range (range = 0.1586) is smaller. Finally, the quantity distribution of the skewness (skewness = −0.13904) is skewed to the left (negative).

Lashgari et al. [14] and this study both found that the size and distribution of the particles were mostly the same but that the sizes and shapes of the particles varied within an appropriate range in our study. However, we found that the particles were not very uniform in terms of size, dimensions, and morphology, which is a crucial factor to consider for future research. To sum up, our results seem to be in line with what Lashgari et al. [14] found about how important it is to look at the uniformity and homogeneity of nanocomposite structures, especially for medical imaging studies like MRI [14].

Also, Tadic et al. [55] look at how hematite nanoparticles are made, their structure and morphology, their magnetic properties, and how they might be used in biomedicine. The study synthesized two different shapes of hematite nanoparticles, rhombohedron and plate-like, and compared their structural, morphological, and magnetic properties. The authors characterized the nanoparticles using various techniques such as XRD, SEM, and magnetic measurements. In comparison to this study, both studies focus on the morphological analysis of nanoparticles using SEM. However, the materials and applications are different. The hematite nanoparticles synthesized in the study have potential biomedical applications for MRI, whereas our work focuses on the fabrication of a nanocomposite for MRI. In terms of methodology, our study segmented the SEM image and used FD analysis to determine the uniformity and homogeneity of the nanoparticles. The study on hematite nanoparticles, on the other hand, used SEM to observe the morphology and size of the nanoparticles. The results showed that the rhombohedron-shaped nanoparticles had a smaller size and a narrower size distribution than the plate-like nanoparticles. The magnetic properties of both shapes were also compared, and the rhombohedron-shaped nanoparticles showed higher magnetic saturation than the plate-like nanoparticles. In total, both studies demonstrate the importance of morphological analysis of nanoparticles for their potential applications. In this work, the use of FD analysis is a novel approach that could be applied to other nanomaterials to determine their uniformity and homogeneity. In several studies, researchers have used different methods, such as FD, for structural and morphological analysis and recommend analyzing the size, dimensions, and morphology of nanomaterials for future research on their structure in terms of uniformity and homogeneity [55].

These findings have important implications for researchers in the fields of material and medical science. FD analysis is a valuable tool for characterizing the properties of nanomaterials and nanocomposites. It provides information on the surface roughness, porosity, and fractal nature of the material, which can be useful for understanding their physical and chemical properties. The use of FD analysis in this study highlights its potential as a nondestructive and noninvasive technique for characterizing nanocomposites for medical imaging applications [56–61].

The results of this study suggest that FD analysis can be used to evaluate the uniformity and homogeneity of nanocomposites for in vitro and in vivo applications, including medical imaging investigations like MRI. By analyzing the size, dimensions, and morphology of the nanocomposites, researchers can gain a better understanding of their structure and properties, which can aid in the design and development of improved materials for medical applications. This study also highlights the importance of carefully analyzing the size, dimensions, and morphology of nanocomposites in order to assess their uniformity and homogeneity, which is critical for their use in medical imaging and other applications. Overall, the findings of this study contribute to our understanding of the properties of nanocomposites and demonstrate the potential of FD analysis as a valuable tool for their characterization.

The study recommended that future research into the structure of nanocomposites should focus on analyzing their size, dimensions, and morphology to improve their uniformity and homogeneity for medical imaging investigations such as MRI. Overall, this study provides insights into the use of fractal analysis to analyze the structure of nanocomposites and highlights the importance of uniformity and homogeneity in their design for medical applications.

4. Conclusion and Interpretations

To our knowledge, this is the first time that a fabricated nanocomposite for MRI has had its SEM image analyzed for FD and other statistical criteria. At the molecular level, the size, dimensions, and morphology of the Gd^{3+}/13X/DOX/FA nanocomposite that was made were measured. This was done to see if the range of particles in the SEM images of the nanocomposites showed that they were uniform and homogeneous. Using a segmented SEM image of the nanocomposite, we were able to determine the FDs of 30 randomly chosen particles and use them to do our calculations. The average, minimum, maximum, skewness, and range of the data were used to analyze the SEM image of the nanocomposite. The fractal data analysis metrics FD_{avg}, FD_{sd}, and FD_{lac} were also used. We evaluated the consistency and uniformity of the SEM image by selecting 30 images. Particle morphology, size, and dimension information all be used to calculate FD. All the data support a negative skewness of −0.13904. Based on FD_{avg}, our maximum and lowest values were 1.9209 and 1.7623. Assuming that the range of the data is limited (in our research, the range is 0.1586), we infer that the particle size and distribution in the SEM image are similar and that these NPs are homogeneous and have high uniformity. The FD_{avg} demonstrates that the average size of our produced NPs is relatively large. To the contrary, we concluded that the particle sizes and shapes are different since this range is not zero, and our data show an appropriate range. The nanocomposite's SEM image supports this interpretation. At first glance, the image seemed to be harmonized. When the computations were run, however, it was discovered that the resulting particles were not very uniform. The particles were evenly distributed throughout all surfaces, yet they varied in size, dimensions, and morphology. In conclusion, the nanocomposite exhibited uniform dispersion across all surfaces despite differences in particle sizes and shapes, as evidenced by several fractal data analysis methods. This highlights the importance of structural analysis in nanoscience and provides valuable information on the morphology and uniformity of nanocomposite materials, particularly for future studies on their homogeneity and consistency, especially in applications such as in vitro and in vivo nanocomposites and medical imaging techniques like MRI.

Data Availability

This article contains all of the data produced or analyzed during this investigation. Any further inquiries should be forwarded to the corresponding author.

Conflicts of Interest

The author declares that he/she has no conflict of interest.

References

[1] C. R. Murthy, B. Gao, A. R. Tao, and G. Arya, "Automated quantitative image analysis of nanoparticle assembly," *Nanoscale*, vol. 7, pp. 9793–9805, 2015.

[2] Y. Khan, H. Sadia, S. Z. A. Shah et al., "Classification, synthetic, and characterization approaches to nanoparticles, and their applications in various fields of nanotechnology: a review," *Catalysts*, vol. 12, no. 11, Article ID 1386, 2022.

[3] K. Ghaderi, F. Akhlaghian, and P. Moradi, "A new robust semi-blind digital image watermarking approach based on LWT-SVD and fractal images," in *2013 21st Iranian Conference on Electrical Engineering (ICEE)*, pp. 1–5, IEEE, Mashhad, Iran, 2013.

[4] A.-J. Shen, D.-L. Li, X.-J. Cai et al., "Multifunctional nanocomposite based on graphene oxide for *in vitro* hepatocarcinoma diagnosis and treatment," *Journal of Biomedical Materials Research Part A*, vol. 100A, pp. 2499–2506, 2012.

[5] S. Ghaderi, K. Ghaderi, and H. Ghaznavi, "Using marker-controlled watershed transform to detect Baker's cyst in magnetic resonance imaging images: a pilot study," *Journal of Medical Signals & Sensors*, vol. 12, no. 1, pp. 84–89, 2022.

[6] S. Ghaderi, B. Divband, and N. Gharehaghaji, "Magnetic resonance imaging property of doxorubicin-loaded gadolinium/13X zeolite/folic acid nanocomposite," *Journal of Biomedical Physics and Engineering*, vol. 10, no. 1, pp. 103–110, 2020.

[7] Z. Atashi, B. Divband, A. Keshtkar et al., "Synthesis of cytocompatible Fe_3O_4@ZSM-5 nanocomposite as magnetic resonance imaging contrast agent," *Journal of Magnetism and Magnetic Materials*, vol. 438, pp. 46–51, 2017.

[8] C. Sun, J. S. H. Lee, and M. Zhang, "Magnetic nanoparticles in MR imaging and drug delivery," *Advanced Drug Delivery Reviews*, vol. 60, no. 11, pp. 1252–1265, 2008.

[9] P. Farinha, J. M. P. Coelho, C. P. Reis, and M. M. Gaspar, "A comprehensive updated review on magnetic nanoparticles in diagnostics," *Nanomaterials*, vol. 11, no. 12, Article ID 3432, 2021.

[10] J. I. Goldstein, D. E. Newbury, J. R. Michael, N. W. M. Ritchie, J. H. J. Scott, and D. C. Joy, "The visibility of features in SEM images," in *Scanning Electron Microscopy and X-Ray Microanalysis*, pp. 123–131, Springer, New York, NY, 2018.

[11] A. N. Kovalenko, "Fractal characterization of nanostructured materials," *Nanosystems: Physics, Chemistry, Mathematics*, vol. 10, no. 1, pp. 42–49, 2019.

[12] L. Squarcina, A. De Luca, M. Bellani, P. Brambilla, F. E. Turkheimer, and A. Bertoldo, "Fractal analysis of MRI data for the characterization of patients with schizophrenia and bipolar disorder," *Physics in Medicine & Biology*, vol. 60, no. 4, Article ID 1697, 2015.

[13] M. Y. Marusina, A. P. Mochalina, E. P. Frolova et al., "MRI image processing based on fractal analysis," *Asian Pacific Journal of Cancer Prevention*, vol. 18, no. 1, pp. 51–55, 2017.

[14] A. Lashgari, S. Ghamami, S. Shahbazkhany, G. Salgado-Morán, and D. Glossman-Mitnik, "Fractal dimension calculation of a manganese-chromium bimetallic nanocomposite using image processing," *Journal of Nanomaterials*, vol. 2015, Article ID 384835, 9 pages, 2015.

[15] B. T. Milne, "Measuring the fractal geometry of landscapes," *Applied Mathematics and Computation*, vol. 27, no. 1, pp. 67–79, 1988.

[16] P. A. Burrough, "Fractal dimensions of landscapes and other environmental data," *Nature*, vol. 294, pp. 240–242, 1981.

[17] D. L. Critten, "Fractal dimension relationships and values associated with certain plant canopies," *Journal of Agricultural Engineering Research*, vol. 67, no. 1, pp. 61–72, 1997.

[18] K. L. Nielsen, J. P. Lynch, and H. N. Weiss, "Fractal geometry of bean root systems: correlations between spatial and fractal dimension," *American Journal of Botany*, vol. 84, no. 1, pp. 26–33, 1997.

[19] A. Husain, J. Reddy, D. Bisht, and M. Sajid, "Fractal dimension of coastline of Australia," *Scientific Reports*, vol. 11, Article ID 6304, 2021.

[20] "Fractal Geometry–an overview | ScienceDirect Topics [Internet]," February 2022, https://www.sciencedirect.com/topics/engineering/fractal-geometry.

[21] P. Asvestas, G. K. Matsopoulos, and K. S. Nikita, "Estimation of fractal dimension of images using a fixed mass approach," *Pattern Recognition Letters*, vol. 20, no. 3, pp. 347–354, 1999.

[22] H. Wang, Z. Yu, X. Cao, and X. Song, "Fractal dimensions of flocs between clay particles and HAB organisms," *Chinese Journal of Oceanology and Limnology*, vol. 29, pp. 656–663, 2011.

[23] D. H. De Bore, "An evaluation of fractal dimensions to quantify changes in the morphology of fluvial suspended sediment particles during baseflow conditions," *Hydrological Processes*, vol. 11, pp. 415–426, 1997.

[24] Y. Feng and Y. Liu, "Fractal dimension as an indicator for quantifying the effects of changing spatial scales on landscape metrics," *Ecological Indicators*, vol. 53, pp. 18–27, 2015.

[25] H. Derakhshankhah, S. Jafari, S. Sarvari et al., "Biomedical applications of zeolitic nanoparticles, with an emphasis on medical interventions," *International Journal of Nanomedicine*, vol. 15, pp. 363–386, 2020.

[26] C.-T. Yang, P. Padmanabhan, and B. Z. Gulyás, "Gadolinium (III) based nanoparticles for T_1-weighted magnetic resonance imaging probes," *RSC Advances*, vol. 6, pp. 60945–60966, 2016.

[27] K. Hanaoka, K. Kikuchi, T. Terai, T. Komatsu, and T. Nagano, "A Gd^{3+}-based magnetic resonance imaging contrast agent sensitive to β-galactosidase activity utilizing a receptor-induced magnetization enhancement (RIME) Phenomenon," *Chemistry – A European Journal*, vol. 14, no. 3, pp. 987–995, 2008.

[28] Y. Liu and N. Zhang, "Gadolinium loaded nanoparticles in theranostic magnetic resonance imaging," *Biomaterials*, vol. 33, no. 21, pp. 5363–5375, 2012.

[29] X. Shen, T. Li, Z. Chen et al., "Luminescent/magnetic PLGA-based hybrid nanocomposites: a smart nanocarrier system for targeted codelivery and dual-modality imaging in cancer

theranostics," *International Journal of Nanomedicine*, vol. 12, pp. 4299–4322, 2017.

[30] S. K. Mishra and S. Kannan, "Doxorubicin-conjugated bimetallic silver–gadolinium nanoalloy for multimodal MRI-CT-optical imaging and pH-responsive drug release," *ACS Biomaterials Science & Engineering*, vol. 3, no. 12, pp. 3607–3619, 2017.

[31] Y. Li, X. Zhi, J. Lin, X. You, and J. Yuan, "Preparation and characterization of DOX loaded keratin nanoparticles for pH/GSH dual responsive release," *Materials Science and Engineering: C*, vol. 73, pp. 189–197, 2017.

[32] S. Hashimoto, "Zeolite photochemistry: impact of zeolites on photochemistry and feedback from photochemistry to zeolite science," *Journal of Photochemistry and Photobiology C: Photochemistry Reviews*, vol. 4, no. 1, pp. 19–49, 2003.

[33] M. Tatlier and A. Erdem-Çenatalar, "Fractal dimension of zeolite surfaces by calculation," *Chaos, Solitons & Fractals*, vol. 12, no. 6, pp. 1145–1155, 2001.

[34] E. Pérez-Botella, S. Valencia, and F. Rey, "Zeolites in adsorption processes: state of the art and future prospects," *Chemical Reviews*, vol. 122, no. 24, pp. 17647–17695, 2022.

[35] C. Feng, K. C. Khulbe, T. Matsuura, R. Farnood, and A. F. Ismail, "Recent progress in zeolite/zeotype membranes," *Journal of Membrane Science and Research*, vol. 1, pp. 49–72, 2015.

[36] S. W. Myint and N. Lam, "A study of lacunarity-based texture analysis approaches to improve urban image classification," *Computers, Environment and Urban Systems*, vol. 29, no. 5, pp. 501–523, 2005.

[37] J. M. Dhivakar, M. S. Babu, R. Sarathi, S. Kornhuber, and N. Chillu, "Investigation on the surface condition of gamma irradiated silicone rubber micro-nanocomposites," *IEEE Access*, vol. 11, pp. 3996–4009, 2023.

[38] M. J. Ostwald and J. Vaughan, "Fractal dimensions in architecture: measuring the characteristic complexity of buildings," in *Handbook of the Mathematics of the Arts and Sciences*, B. Sriraman, Ed., pp. 1–17, Springer, Cham, 2018.

[39] A. A. Rezaie and A. Habiboghli, "Detection of lung nodules on medical images by the use of fractal segmentation," *International Journal of Interactive Multimedia and Artificial Intelligence*, vol. 4, no. 5, pp. 15–19, 2017.

[40] A. K. Bisoi and J. Mishra, "On calculation of fractal dimension of images," *Pattern Recognition Letters*, vol. 22, no. 6-7, pp. 631–637, 2001.

[41] B. B. Mandelbrot, *The Fractal Geometry of Nature*, Vol. 1, W. H. freeman, New York, 1982.

[42] L. M. Alves, "Foundations of measurement fractal theory for the fracture mechanics," in *Applied Fracture Mechanics*, A. Belov, Ed., IntechOpen, 2012.

[43] L. Debnath, "A brief historical introduction to fractals and fractal geometry," *International Journal of Mathematical Education in Science and Technology*, vol. 37, no. 1, pp. 29–50, 2006.

[44] F. J. Molz, H. Rajaram, and S. Lu, "Stochastic fractal-based models of heterogeneity in subsurface hydrology: origins, applications, limitations, and future research questions," *Reviews of Geophysics*, vol. 42, no. 1, 2004.

[45] M. Manera, B. S. Dezfuli, C. Borreca, and L. Giari, "The use of fractal dimension and lacunarity in the characterization of mast cell degranulation in rainbow trout (*Oncorhynchus mykiss*)," *Journal of Microscopy*, vol. 256, no. 2, pp. 82–89, 2014.

[46] D. Sebők, L. Vásárhelyi, I. Szenti, R. Vajtai, Z. Kónya, and Á. Kukovecz, "Fast and accurate lacunarity calculation for large 3D micro-CT datasets," *Acta Materialia*, vol. 214, Article ID 116970, 2021.

[47] M. Muchtar, N. Suciati, and C. Fatichah, "Fractal dimension and lacunarity combination for plant leaf classification," *Jurnal Ilmu Komputer dan Informasi*, vol. 9, no. 2, pp. 96–105, 2016.

[48] F. Albregtsen and B. Nielsen, "Fractal dimension and lacunarity estimated by sequential 1D polygonization of 2D images," in *Theory and Applications of Image Analysis II*, pp. 79–88, World Scientific, 1995.

[49] M. Bouda, J. S. Caplan, and J. E. Saiers, "Box-counting dimension revisited: presenting an efficient method of minimizing quantization error and an assessment of the self-similarity of structural root systems," *Frontiers in Plant Science*, vol. 7, Article ID 149, 2016.

[50] P. Rambabu and C. Naga Raju, "The optimal thresholding technique for image segmentation using fuzzy Otsu's method," *International Journal of Applied Engineering Research*, vol. 10, no. 13, pp. 33842–33846, 2015.

[51] Y. B. Chen and O. T.-C. Chen, "Image segmentation method using thresholds automatically determined from picture contents," *EURASIP Journal on Image and Video Processing*, vol. 2009, Article ID 140492, 2009.

[52] S. L. Bangare, A. Dubal, P. S. Bangare, and S. T. Patil, "Reviewing Otsu's method for image thresholding," *International Journal of Applied Engineering Research*, vol. 10, no. 9, pp. 21777–21783, 2015.

[53] J. Rogowska, "Overview and fundamentals of medical image segmentation," in *Handbook of Medical Image Processing and Analysis*, I. N. Bankman, Ed., pp. 73–90, Academic Press, 2nd edition, 2009.

[54] S. K. Mitra and G. L. Sicuranza, *Nonlinear Image Processing*, Academic Press, 2001.

[55] M. Tadic, L. Kopanja, M. Panjan et al., "Rhombohedron and plate-like hematite (α-Fe2O3) nanoparticles: synthesis, structure, morphology, magnetic properties and potential biomedical applications for MRI," *Materials Research Bulletin*, vol. 133, Article ID 111055, 2021.

[56] M. Tadic, S. Kralj, and L. Kopanja, "Synthesis, particle shape characterization, magnetic properties and surface modification of superparamagnetic iron oxide nanochains," *Materials Characterization*, vol. 148, pp. 123–133, 2019.

[57] M. Tadic, D. Trpkov, L. Kopanja, S. Vojnovic, and M. Panjan, "Hydrothermal synthesis of hematite (α-Fe_2O_3) nanoparticle forms: synthesis conditions, structure, particle shape analysis, cytotoxicity and magnetic properties," *Journal of Alloys and Compounds*, vol. 792, pp. 599–609, 2019.

[58] A. M. Guryanov and S. A. Guryanov, "Nanoscale control of hydrated portland cement structure," *Solid State Phenomena*, vol. 335, pp. 159–165, 2022.

[59] Q. Jiang, Q. Zhang, X. Wu, L. Wu, and J. H. Lin, "Exploring the interfacial phase and π–π stacking in aligned carbon nanotube/polyimide nanocomposites," *Nanomaterials*, vol. 10, no. 6, Article ID 1158, 2020.

[60] A. Zuliani, D. Chelazzi, R. Mastrangelo, R. Giorgi, and P. Baglioni, "Adsorption kinetics of acetic acid into ZnO/castor oil-derived polyurethanes," *Journal of Colloid and Interface Science*, vol. 632, no. Pt A, pp. 74–86, 2023.

[61] C. Appel, B. Kuttich, L. Stühn, R. W. Stark, and B. Stühn, "Structural properties and magnetic ordering in 2D polymer nanocomposites: existence of long magnetic dipolar chains in zero field," *Langmuir*, vol. 35, no. 37, pp. 12180–12191, 2019.